JOURNAL OF MATERIALS SCIENCE **33** (1998) 5049–5058

The measurement of compressive creep deformation and damage mechanisms in a single-phase alumina

Part II *Correlation of creep cavitation and grain boundary sliding*

C. R. BLANCHARD, R. A. PAGE
Southwest Research Institute, San Antonio, TX 78228, USA
E-mail: cblanchard@swri.org

S. SPOONER
Oak Ridge National Laboratory, Oak Ridge, TN 37831, USA

It has been theorized that stochastic grain boundary sliding (GBS) is the primary driving force for the nucleation, growth, and coalescence of cavities located on the grain boundaries of polycrystalline ceramics undergoing creep. This paper reports on the results of co-ordinated measurements of both GBS and creep cavitation during the creep of a single-phase alumina. Constant compressive stress creep experiments were performed at a temperature of 1600 °C, and stress levels of 70, 100, and 140 MPa. Small angle neutron scattering measurements (SANS) show that cavities nucleate continuously due to creep at all three stress levels, and that since negligible cavity growth was measured, creep cavitation appears to be ruled by a nucleation rather than a growth process. Also, at a constant creep temperature, the number and volume of cavities measured was observed to decrease with a decrease in the applied stress. GBS displacements reported in Part 1 of this paper [1] are related to the number of cavities nucleated per unit volume and shown to relate directly, thereby providing experimental evidence that GBS may act as the driving force for creep cavitation.

1. Introduction

The bulk damage process due to creep observed in structural ceramics generally includes the stress-induced nucleation, growth, and coalescence of cavities located on grain boundaries [2–4]. These cavitation events eventually lead to crack formation and mechanical failure, either through bulk damage accumulating to form a critical flaw [5], or through the formation of a microcrack which grows subcritically (through continuous cavity nucleation) eventually leading to failure [5, 6]. Parameters such as applied stress, temperature, environment, and microstructure have been shown to affect the specific mechanisms by which advanced ceramics fail because of creep damage [7, 8].

In striving to understand and predict creep damage and failure in ceramics, researchers have studied and modelled the creep cavity [9–12] and creep crack [5, 6, 13–15] nucleation and growth processes. Although these works represent significant progress in understanding damage and failure due to creep, for eventual component lifetime prediction, creep cavitation in structural ceramics must be understood in terms of its process driving force. Grain boundary sliding (GBS) has been suggested as the driving force for creep cavitation, whereby stress concentrations arise at various critical areas, such as triple points, second-phase particles, and ledges on the grain boundaries providing the required local tensile stress for cavity nucleation and growth to occur [9, 16–18]. Previously, direct experimental evidence supporting the hypothesis that GBS is the driving force for creep cavitation has been published only for metal bicrystals or very large polycrystals undergoing creep [19, 20]. As early as 1959, Intrater and Machlin [19] reported that during a GBS study on copper bicrystals, they observed the number of cavities nucleated to increase linearly with increasing GBS displacement. They also noted that the cavities nucleated at ledges created on the grain boundaries by slip planes. In a later experiment, Fleck *et al.* [20] measured the number of cavities per unit area to increase linearly with the magnitude of GBS displacement on copper polycrystals with a 530 μm grain size. In addition, they also noted that each cavity observed was associated with a grain boundary particle and that an incubation time was required before cavity nucleation was detected. This incubation time was related directly to a critical GBS displacement.

Although numerous GBS and creep cavitation studies have been reported and reviewed in the metallurgy literature [21, 22], there are only a few reports in the literature of GBS [23–35] and creep cavitation [4, 12, 36–38] measurements performed on ceramic materials. The primary goal of the majority of the GBS measurements reported [26–35] was to determine the overall contribution of GBS to the total creep strain of the ceramic specimen. The GBS behaviour, kinetics, and effect on the resultant cavitation processes were not investigated. As such, GBS has historically been regarded primarily as a deformation mechanism in ceramic materials, and not studied as a potential driving force to the damage and failure processes observed during creep.

Recently, Blanchard and Page [1, 23–25] reported on a new measurement technique using a machine vision system that enables the measurement of GBS displacements on individual polycrystalline grain boundaries with respect to creep time. Initial measurements were performed on a single-phase alumina undergoing creep at a temperature of 1600 °C and a stress of 140 MPa. These data showed that GBS in a ceramic is history independent over creep time on individual boundaries and that GBS is a stochastic process. These findings support previous contentions [39, 40] that GBS provides a transient driving force for a continuous cavitation process. In addition, Blanchard and Page [24] calculated strains resulting from GBS on individual grain boundaries reaching 4000% (corresponding to a strain rate of $2 \times 10^{-2}\,s^{-1}$). The measurement of these large grain boundary strains provided preliminary experimental evidence supporting calculations performed by Raj [16] and Argon *et al.* [9], who showed that localized stresses 5 to 20 times the remote applied stress were required in order to nucleate stable creep cavities. Raj [16] and Argon *et al.* [9] also concluded that GBS was required in order to generate those localized stress concentrations.

In order to relate GBS to the creep cavitation phenomenon, effectively simultaneous measurements of both processes during a given experiment would be required. Until recently, obtaining statistically significant creep cavitation data has been difficult. Microscopy techniques on fracture surfaces (scanning electron microscopy; SEM) or thinned material sections (transmission electron microscopy; TEM) have been used to provide information regarding cavity shape, spacing, and location, and on the evidence of microstructural features associated with the creep cavities such as grain boundary ledges [41]. However, the very small sampling dimensions allowed on a fracture surface or thin foil do not provide statistically significant data regarding cavitation behaviour in the material bulk. Precision density measurements, while providing the total cavity volume, do not allow one to distinguish between the cavity nucleation and growth processes. The only experimental technique that can measure microstructural changes of the size of a nucleation event (2–200 nm) [12] and distinguish between the cavity nucleation and growth processes by measuring the number and size of the cavities on a statistically significant scale, is small-angle neutron scattering (SANS).

SANS offers a number of advantages in performing detailed studies of creep cavitation in metals and ceramics, as pointed out by Chan and Page [6]. Specifically, neutrons have a low absorption and may thus penetrate sufficiently thick samples to provide data from a volume sizeable enough to result in statistically significant data. In addition, because neutrons are available with relatively long wavelengths, double diffraction is avoided. Finally, SANS permits the measurement of total volume, number, and size of the scattering centres, which in this case are creep cavities.

It has been demonstrated that SANS is in fact a powerful tool for characterizing creep cavitation in metals [42], and more recently in ceramics [4, 12, 36–38]. In fact, the extensive work in characterizing creep cavitation in ceramics by Page and co-workers [4, 12, 36–38] has revealed unexpected results that confirm the importance of understanding the nucleation, growth, and coalescence processes in a variety of ceramics covering a range of stress and temperature. For example [12], although creep cavitation was observed in all three materials studied, cavitation in a low-stressed, glassy-phase AD99 Al_2O_3 (AD99 Alumina, Coors Porcelain Co., Golden, CO) and a single-phase Al_2O_3 (Lucalox®, General Electric Lamp Glass Division, Cleveland, OH) material was found to be nucleation-controlled where cavities nucleated continuously with little subsequent growth. On the other hand, it was observed that NC203 SiC (NC203 SiC, Norton Company, Worcester, MA) cavitated during creep through a growth-dominated process where cavity nucleation took place early in the creep process, but the ultimate lifetime was controlled by cavity growth and coalescence.

The purpose of this paper is to present creep cavitation measurements from experiments performed at a temperature of 1600 °C and at stress levels of 140, 100 and 70 MPa on a single-phase alumina, and to correlate these results with the GBS measurements reported previously in Part 1 of this paper [1]. The GBS measurements made on individual grain boundaries over creep time were reported [1] to provide further insight into the GBS process and were discussed in terms of the GBS kinetics. Although similar cavitation measurements using SANS have been performed, this paper will include new data which corresponds directly to the GBS measurements reported. As such, the GBS and creep cavitation phenomena will be related.

2. Experimental procedure

2.1. Material

Lucalox® Al_2O_3, with an average grain size of 17 μm, was selected for this study because of its relatively large equiaxed grains and glass-free grain boundaries, characteristics which together provided for fewer complications when digitizing the microstructures. Lucalox® is composed of 99.9% pure Al_2O_3 doped with MgO as a sintering aid. Although $MgAl_2O_4$ spinel particles have been identified at triple points [43], the microstructure of Lucalox® is relatively clean and free from any glassy phase or regular second-phase precipitates.

2.2. Specimen preparation

Compressive creep specimens were machined into right circular cylinders, 1.27 cm in length and 0.64 cm in

diameter. The specimen ends were ground and lapped flat and parallel to within 5 μm.

For the purpose of characterizing creep cavitation, the right circular cylinder creep specimens were creep tested (to be described) as-machined. After compressive creep testing, 0.5×1.27 cm flats were ground and polished to a mirror-finish on opposing sides of each compression specimen. This provided specimens approximately 0.39 cm thick for SANS measurements.

2.3. Creep tests

Compressive creep tests were performed on the as-sintered, machined specimens in a titanium-gettered argon atmosphere at 1600 °C using a dead-weight-loaded machine. Specimens were tested under stress levels of 140, 100 and 70 MPa for creep cavitation measurements.

In order to perform the desired GBS measurements with respect to creep time (as described in Part 1 [1] of this paper), the creep tests were interrupted periodically, thereby effectively thermally cycling the samples. Therefore, in order to be able to compare directly the creep cavitation and GBS measurements, the creep tests performed for SANS characterization were thermally cycled identically to those tests performed for the GBS measurements. Specifically, the 140 MPa tests were run in 30-min cycles, where the specimen was heated to 1600 °C, loaded for 30 min, and cooled under load. Four specimens were crept at 140 MPa for 1, 2, 3 and 4 30-min cycles, respectively. The 100 MPa tests were run for 1, 2, 3 and 7 60-min cycles, and the 70 MPa tests were run for 1, 2 and 3 180-min cycles. Also, one specimen was tested under a 70 MPa load for 1080 min to observe the creep cavitation behaviour at a larger strain level.

2.4. Cavitation measurements

The cavitation measurements were performed on the 30 m small-angle neutron scattering spectrometer at the National Center for Small-Angle Scattering Research at Oak Ridge National Laboratory (ORNL). A description of the facility has been given by Koehler [44]. A bank of pyrolytic graphite crystals provided an incident neutron wavelength, λ, to the samples of 0.475 nm. The scattered neutron intensities were measured on a position sensitive 64×64 cm detector with resolution element dimensions of 1×1 cm. The detector was centered around a beam stop to arrest the primary transmitted beam. The incident and scattered neutron beams both traveled in evacuated paths. The experiments were performed at sample-to-detector distances of 6 m and 16.12 m. These two detector positions resulted in intensity measurements at scattering vectors, q, from 0.041 nm^{-1} to 0.700 nm^{-1} where $q = 4\pi \sin\theta_B/\lambda$ and θ_B is the Bragg angle. The measured neutron intensities were corrected, as described by Blanchard [25], for unwanted background arising from electronic background, scattering from the sample holder, and scattering from the baseline microstructure. The corrected scattering intensities were radially averaged and converted to a macroscopic differential scattering cross section, $d\Sigma/d\Omega$, by normalizing the data to a well-characterized irradiated aluminium sample containing voids with a known scattering cross section [45, 46]. The normalization procedure to obtain $d\Sigma/d\Omega$ versus q is described in detail by Hendricks *et al.* [45].

2.5. Density measurements

Because the SANS data did not extend completely into the Guinier scattering region (the importance of which will be discussed later), precision density measurements were performed to obtain the cavity volume in each specimen. In order to measure accurately such small changes in specimen density, a technique based on Archimedes' principle was used, as described by Ratcliffe [47]. Measurements were performed by weighing an uncrept blank specimen and the crept specimens both in air and diethylphthalate. The immersed weights were obtained using a flask with a copper cylinder surrounding the specimen to reduce thermal gradients. The density changes resulting from creep, $\Delta\rho/\rho$, were then calculated as follows

$$\frac{\Delta\rho}{\rho} = 1 - \frac{W(w - w_1)}{w(W - W_1)} \tag{1}$$

where W and w are the weight of the crept specimen and the uncrept blank in air, respectively, and W_1 and w_1 are the weight of the crept specimen and uncrept blank in liquid, respectively. This technique provided for measurements of density changes on the order of 1 part in 10^6.

3. Creep cavitation results and analysis

3.1. Scattering curves

The effect of creep on the scattering curves, $\ln(d\Sigma/d\Omega)$ versus q, is shown in Fig. 1. When compared to the uncrept baseline specimen, the specimen crept for 420 min under a 100 MPa load exhibited a significant increase in scattering. In addition, data gathered at both

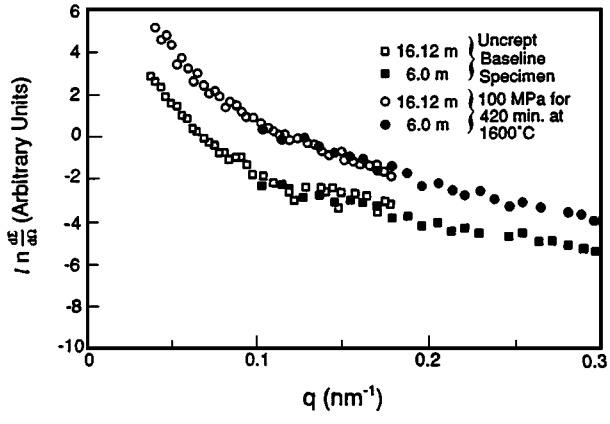

Figure 1 Differential scattering cross section, $d\Sigma/d\Omega$, as a function of the scattering vector, q, for an uncrept baseline specimen and a specimen crept under a 100 MPa stress for 480 min. An increase in scattering due to creep cavitation and good overlap of data at both detector positions is demonstrated.

detector positions are plotted to show the good agreement obtained in the region where there is a q overlap. These data are representative of all the SANS measurements made on the crept specimens.

A number of microstructural features, such as precipitates, pre-existing pores, and grain boundaries, could contribute to the increase in scattering at small angles. Therefore, it was necessary to determine if microstructural features other than creep cavities contributed to the differential scattering cross-section. Page *et al.* [37] performed a SANS study on Lucalox® alumina crept under similar conditions used in this study. They concluded that creep cavities were the only microstructural feature that contributed significantly to scattering at small angles. It is therefore assumed that all increases in $d\Sigma/d\Omega$ measured in this study may be attributed to creep cavitation.

3.2. Radius of gyration

As shown in Fig. 2, the SANS data were observed to follow Guinier's law [48] at small values of q, specifically, for $q \leq 0.063\ \text{nm}^{-1}$, $\ln(d\Sigma/d\Omega)$ is proportional to q^2. In the Guinier region, the differential scattering cross-section can be expressed as

$$\ln \frac{d\Sigma}{d\Omega} = \ln A - \frac{q^2 R_G^2}{3} \tag{2}$$

where A is a constant and R_G is the radius of gyration. The radius of gyration may further be defined as

$$R_G^2 = \frac{3\langle R^8 \rangle}{5\langle R^6 \rangle} \tag{3}$$

where R is the spherical cavity radius for a group of spherical cavities with a distribution of sizes and $\langle\rangle$ represents an average over all of the cavities. The radius of gyration was found by determining the slope of the $\ln(d\Sigma/d\Omega)$ versus q^2 line, m_G, at low q values as follows

$$m_G = \frac{-R_G^2}{3} \tag{4}$$

The values listed for R_G, obtained by fitting the experimental data using linear regression to Equation 4, are listed in Table I. The reader should note that the data were not observed to extend completely into the Guinier region (as will be discussed later). This could result in an underestimation of the true value of R_G. Within the error of measurement, the radius of gyration appears to remain relatively constant at a value of ≈ 54 nm over all three stress levels at varying test times. This is demonstrated in Fig. 3, where R_G is plotted versus strain for the specimens tested at 140, 100 and 70 MPa. Page *et al.* [37] also observed that R_G remained constant in Lucalox® tested under similar conditions, although at a slightly larger value of ~ 60 nm. Note, though, that Page *et al.* [37] performed their SANS measurements down to $q = 0.036\ \text{nm}^{-1}$, slightly smaller than the lower limit of $q = 0.041\ \text{nm}^{-1}$ used in these experiments. The data gathered by Page *et al.* [37] likely extended further into the Guinier region, thereby likely providing a more accurate estimate of R_G.

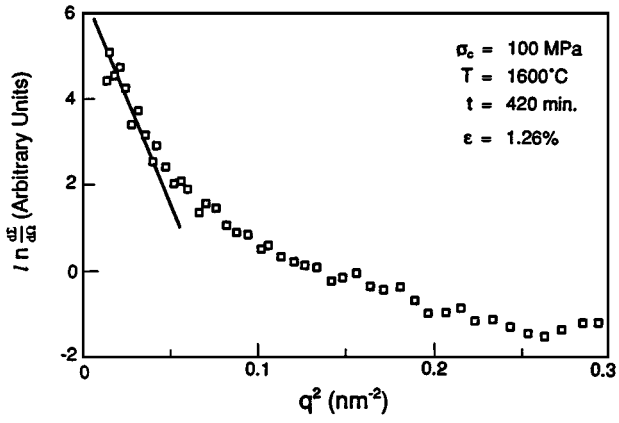

Figure 2 $\ln d\Sigma/d\Omega$ versus q^2 for a specimen crept under a load of 100 MPa illustrating the Guinier region at low values of q.

TABLE I Creep cavitation measurements

Applied stress (MPa)	Grain size (μm)	ϵ (%)	R_G (nm)	R_p (nm)	R_p[a] (nm)	V_c/V	V_c/V[a]	N_c/V (cm^{-3})	N_c/V[a] (cm^{-3})
140	17	0.14	54	[b]	[b]	[b]	8.0×10^{-5}	[b]	[b]
140	17	0.36	54	84	959	6.8×10^{-5}	7.7×10^{-4}	2.7×10^{11}	2.1×10^{9}
140	17	0.88	57	80	453	1.9×10^{-4}	1.1×10^{-3}	8.8×10^{11}	2.8×10^{10}
140	17	1.08	54	65	1050	5.1×10^{-5}	8.3×10^{-4}	4.4×10^{11}	1.7×10^{9}
100	17	0.14	53	186	3042	1.3×10^{-5}	2.1×10^{-4}	4.7×10^{9}	1.8×10^{7}
100	17	0.36	48	80	1484	1.4×10^{-5}	2.6×10^{-4}	6.5×10^{10}	1.9×10^{8}
100	17	0.48	57	86	1224	2.2×10^{-5}	3.1×10^{-4}	8.2×10^{10}	4.0×10^{8}
100	17	1.26	55	73	822	2.1×10^{-4}	2.4×10^{-3}	1.3×10^{12}	1.0×10^{10}
70	17	0.47	51	52	592	2.1×10^{-5}	2.4×10^{-4}	3.5×10^{11}	2.7×10^{9}
70	17	0.86	55	71	392	6.8×10^{-5}	3.7×10^{-4}	4.4×10^{11}	1.5×10^{10}
70	17	1.00	55	73	756	4.1×10^{-5}	4.2×10^{-4}	2.5×10^{11}	2.3×10^{9}
70	17	5.50	55	82	1189	2.6×10^{-4}	3.8×10^{-3}	1.1×10^{12}	5.3×10^{9}

[a]Obtained from precision density measurements.
[b]No data was obtained due to the very low signal-to-noise ratio within the Porod region in SANS data.

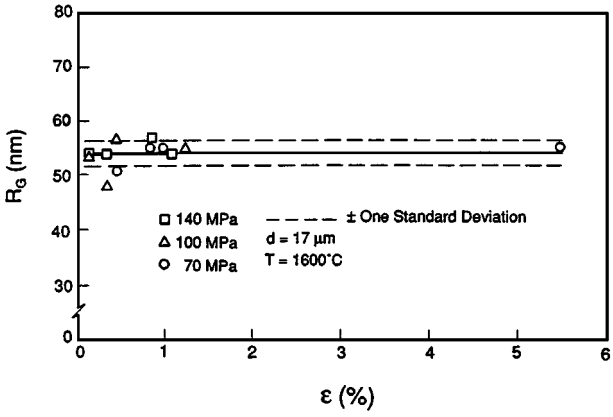

Figure 3 Radius of gyration versus specimen strain for specimens tested at 140, 100 and 70 MPa.

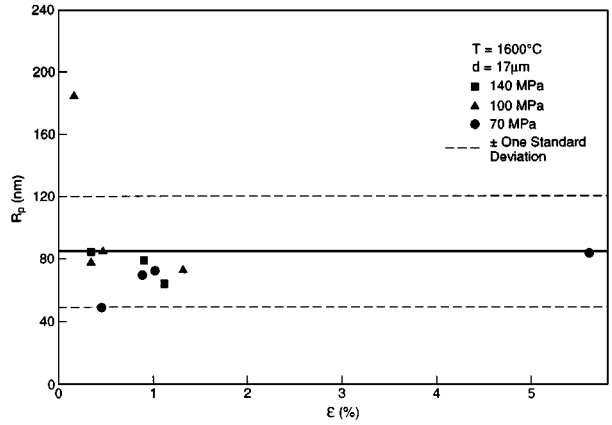

Figure 5 Porod radius versus specimen strain for specimens tested at 140, 100 and 70 MPa.

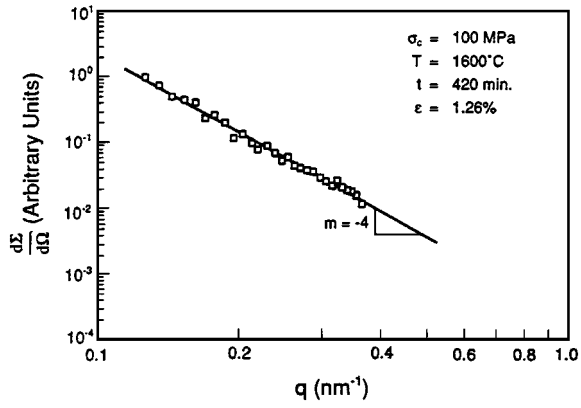

Figure 4 Log $d\Sigma/d\Omega$ versus log q for a specimen crept under a load of 100 MPa illustrating Porod behavior at high values of q.

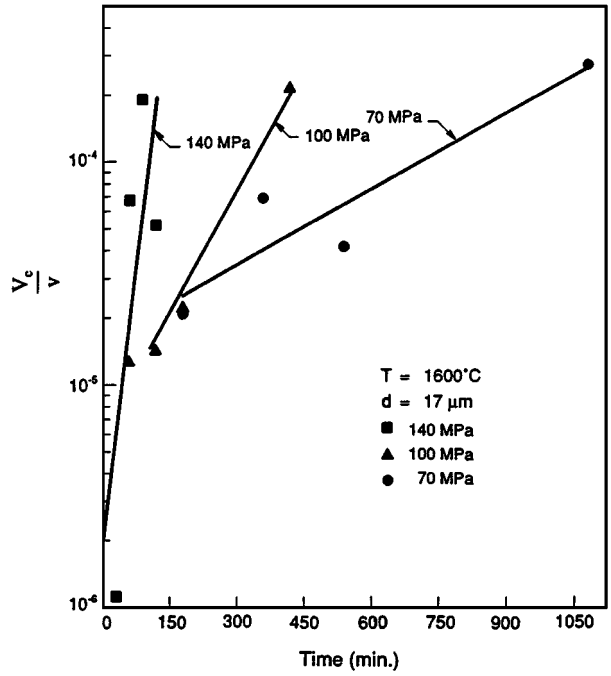

Figure 6 Cavity volume fraction versus creep time for specimens tested at 140, 100 and 70 MPa. The solid lines represent a least-squares fit.

3.3. Porod radius and the invariant

As shown in Fig. 4, the SANS data were observed to follow Porod's law [49] at high values of q, specifically where $\ln(d\Sigma/d\Omega)$ is proportional to q^{-4}. Because the data were measured in both the Porod and Guinier regions, the invariant and Porod constant were evaluated and used to determine the Porod radius (R_p) as follows

$$R_p = \frac{3}{\pi}\left(\int_0^\infty \frac{d\Sigma}{d\Omega} q^2 dq\right)\left(\lim_{q\to\infty} q^4 \frac{d\Sigma}{d\Omega}\right)^{-1} = \frac{3}{\pi}\frac{Q_0}{P} \quad (5)$$

where Q_0 is the invariant and P is the Porod constant. The invariant was evaluated by numerically integrating the scattering data. Values of $d\Sigma/d\Omega$ were obtained by extrapolating into the Guinier and Porod regions. The definition of the Porod constant is the limit of q^4 $(d\Sigma/d\Omega)$ as q approaches infinity. The values of R_p calculated in this way are listed in Table I. Fig. 5 demonstrates that the value of R_p remains essentially constant with respect to specimen strain for all three test loads. Since the two measures of cavity size, R_G and R_p, remained constant at all three stress levels, negligible cavity growth was observed at these test conditions.

3.4. Cavity volume fraction

The volume fraction of creep cavities, V_c/V, was found using the following equation

$$\frac{V_c}{V} = \frac{1}{2\pi^2(\Delta\rho_s)^2}\int_0^\infty \frac{d\Sigma}{d\Omega} q^2 dq \quad (6)$$

where $\Delta\rho_s$ is the difference in scattering length density between a cavity and dense Al_2O_3 ($\Delta\rho_s = 5.75 \times 10^{10}$ cm^2). The cavity volume fraction determined in this manner is plotted versus creep time in Fig. 6 and versus creep strain in Fig. 7 for all three test loads. In addition, these values are listed in Table I.

The cavity volume fraction is observed to increase linearly with creep time, as shown in Fig. 6. In addition, the slope of the least-squares line was observed to decrease as the applied stress decreased from 140 to 70 MPa. When plotted versus specimen strain (ϵ) (Fig. 7), V_c/V was also observed to increase linearly

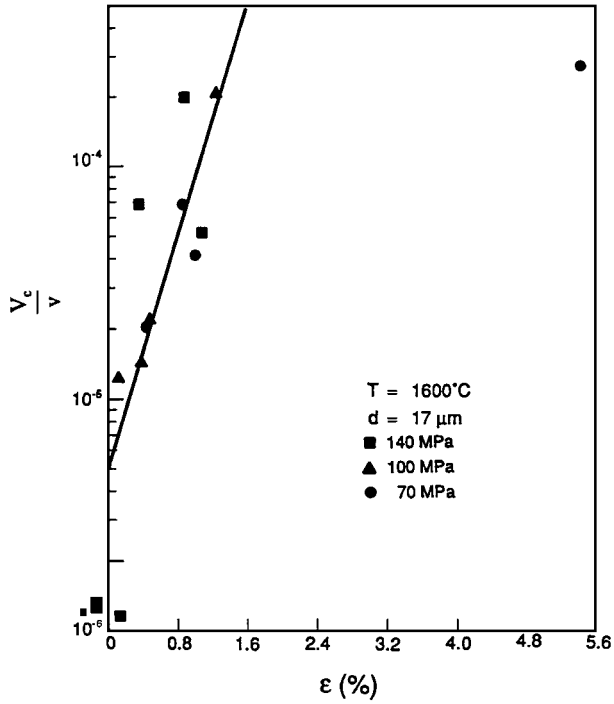

Figure 7 Cavity volume fraction versus creep strain for specimens tested at 140, 100 and 70 MPa. The solid line represents a least-squares fit of the data excluding the point at a strain of 5.5%.

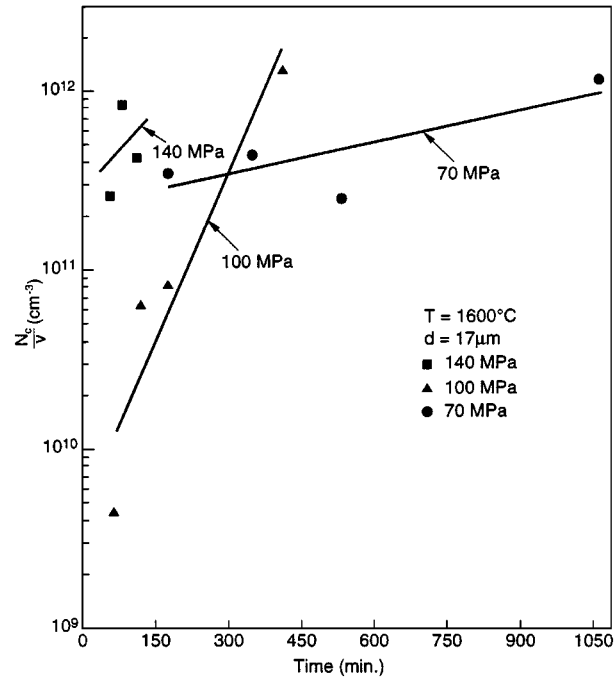

Figure 8 The number of cavities per unit volume versus creep time for specimens tested at 140, 100 and 70 MPa. The solid lines represent a least-squares fit.

(with the exception of the point at $\epsilon = 5.5\%$) with the least-squares line fit to the data produced at all three test loads. As observed in Fig. 7, strain was found to normalize the effect of stress on V_c/V. Page *et al.* [37] have also observed linearly increasing relationships between V_c/V versus time and strain in Lucalox® tested under similar conditions.

3.5. Cavity number

The number of cavities per unit volume, N_c/V, was obtained as follows [37]

$$\frac{N_c}{V} = \frac{3V_c}{4\pi V R_p^3} \tag{7}$$

The values of N_c/V calculated in this manner are listed in Table I. The number of cavities per unit volume is plotted versus creep time in Fig. 8 and versus creep strain in Fig. 9. N_c/V is shown to increase linearly with time for the 140, 100 and 70 MPa test loads, although the slopes were observed to decrease dramatically between 100 and 70 MPa. When plotted versus creep strain in Fig. 9, N_c/V appears to exhibit a linearly increasing behaviour with all three test loads (again with the exception of the point $\epsilon = 5.5\%$) with strain once again normalizing the effect of stress. Again, previous work by Page *et al.* [37] has shown linearly increasing N_c/V with both creep time and strain in Lucalox® tested under similar conditions.

3.6. Density measurement results

The results of the precision density measurements are shown in Fig. 10 as V_c/V versus specimen strain for

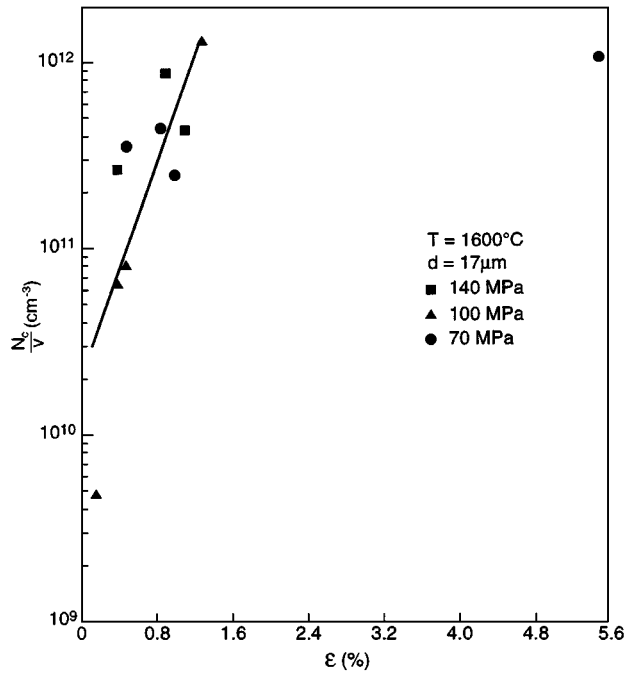

Figure 9 The number of cavities per unit volume versus creep strain for specimens tested at 140, 100 and 70 MPa. The solid line represents a least-squares fit of the data excluding the point at a strain of 5.5%.

the specimens tested at 140, 100 and 70 MPa. Values of V_c/V are observed to increase linearly with creep strain as with the values of V_c/V obtained using SANS measurements (Fig. 7). Although, when referring to Table I, where values of V_c/V obtained from both density and SANS measurements are listed, it is apparent that a larger volume fraction of cavities resulted from the density measurements compared to the SANS measurements, in most cases, an order of magnitude larger. It is hypothesized that the larger values of V_c/V obtained by

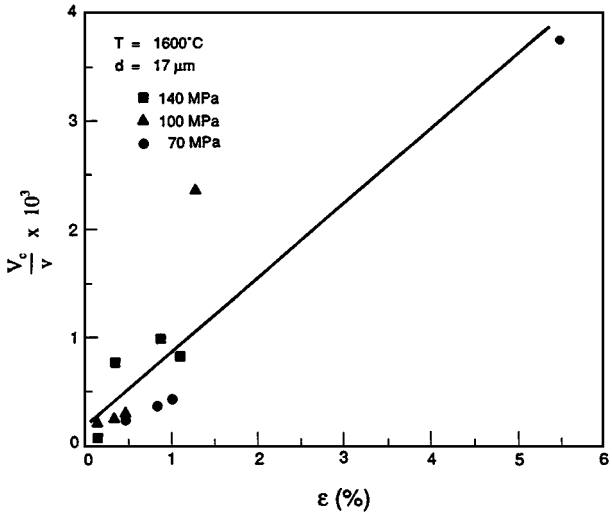

Figure 10 The cavity volume fraction obtained from precision density measurements versus creep strain for specimens tested at 140, 100 and 70 MPa.

the density measurements suggest the presence of larger cavities, possibly caused by cavity growth and coalescence, and possibly some grain boundary cracks, which lie above the cavity size detection limit of the SANS technique ($\sim$ 0.3–0.5 μm). Support for this hypothesis is found by referring to the photomicrographs of the cavitated microstructures of these specimens after creep testing [41], which documented the existence of many cavities equal to or greater than 0.5 μm in diameter.

The values of V_c/V generated from the density measurements were also used to calculate the invariant for each specimen using Equation 6, and the Porod radius was recalculated using Equation 5. Values of R_p calculated in this manner are listed in Table I and are plotted versus specimen strain for specimens tested at 140, 100 and 70 MPa in Fig. 11. The Porod radius found using density measurements also remained constant with strain, as with the R_p values obtained using SANS data (Fig. 5), although the magnitudes of R_p values were generally an order of magnitude larger than those calculated from SANS data. These larger R_p values are expected based on the larger V_c/V values obtained from the precision density measurements.

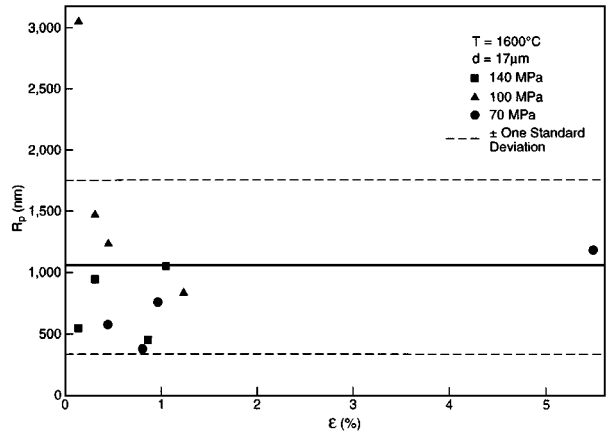

Figure 11 Porod radius determined from precision density measurements versus specimen strain for the specimens tested at 140, 100 and 70 MPa.

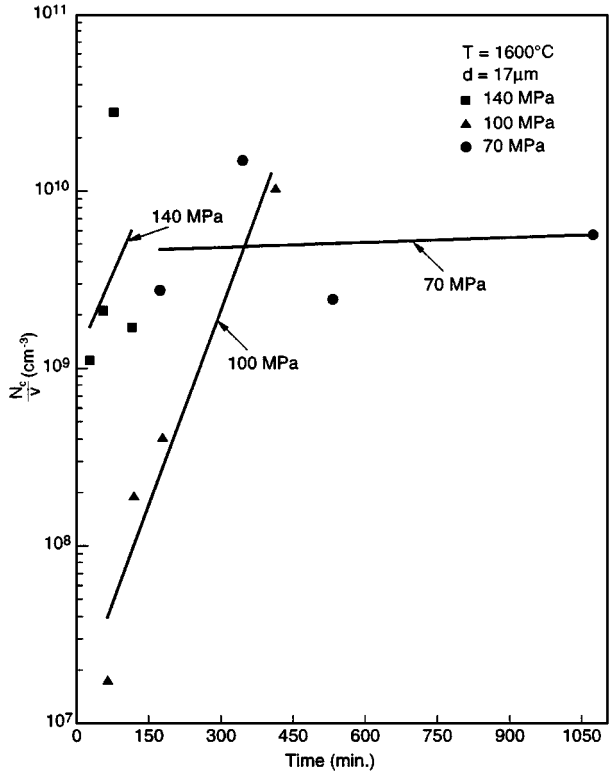

Figure 12 The number of cavities per unit volume versus creep time obtained from precision density measurements for specimens tested at 140, 100 and 70 MPa. The solid lines represent a least-squares fit.

Values of N_c/V were also calculated from the precision density data using Equation 7. These data are listed in Table I and are plotted versus creep time in Fig. 12. The trends are similar to those observed using SANS data (Fig. 8). Specifically N_c/V is observed to increase linearly with time for all three test loads, and the slopes of the least-squares fits decrease between 100 and 70 MPa. Therefore, although the actual values obtained for V_c/V, R_p and N_c/V were different using SANS and precision density measurements, the trends observed in the precision density data support the data obtained from SANS measurements.

3.7. GBS and cavitation measurements

Based on previous modelling efforts and limited experimental data from metal bicrystals, it has been hypothesized that GBS provides the driving force for creep cavitation in ceramic materials undergoing creep. Experimental evidence supporting this hypothesis is shown in Fig. 13 as the number of cavities measured per unit volume versus the corresponding GBS displacement (cumulative average $\overline{dy}_{GB}$) measured on comparable Lucalox® specimens undergoing creep at stresses of 140 and 70 MPa. Although there is some scatter in the data, the number of cavities per unit volume appears to increase with increasing cumulative average $\overline{dy}_{GB}$ measured for corresponding test times. Because the relationships between both N_c/V (Fig. 8) and $\overline{dy}_{GB}$ [1] with time were linear, a least-squares linear approximation was used to describe the observed trend of increasing N_c/V with $\overline{dy}_{GB}$. The lines resulting from the

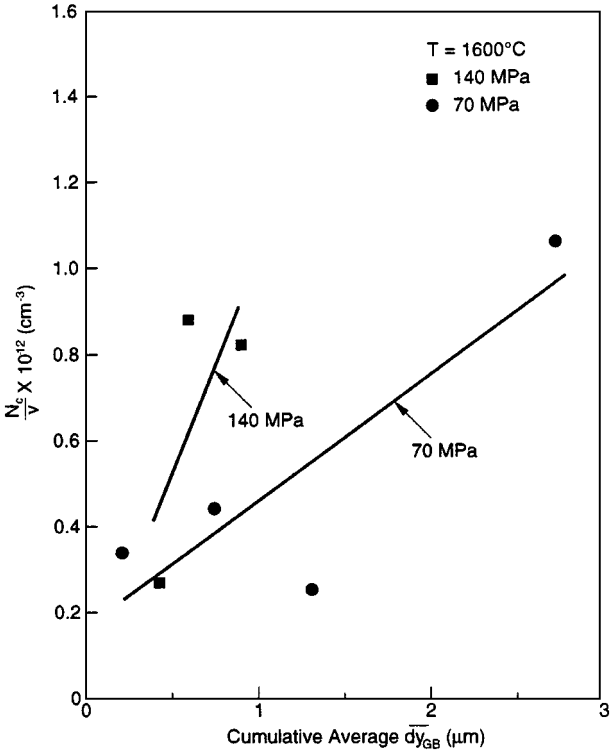

Figure 13 Number of cavities per unit volume versus the corresponding cumulative average $\overline{dy}_{GB}$.

least-squares analysis are as follows for the 140 and 70 MPa tests.

140 MPa

$$\frac{N_c}{V} = 1.0 \times 10^{12}\ \text{cm}^{-3}\ \mu\text{m}^{-1}\overline{dy}_{GB} + 1.8 \times 10^{10}\ \text{cm}^{-3} \tag{8}$$

70 MPa

$$\frac{N_c}{V} = 2.9 \times 10^{11}\ \text{cm}^{-3}\ \mu\text{m}^{-1}\overline{dy}_{GB} + 1.6 \times 10^{11}\ \text{cm}^{-3} \tag{9}$$

The direct correspondence between N_c/V and $\overline{dy}_{GB}$ supports the contention that GBS is the driving force for creep cavitation.

4. Discussion

4.1. Creep cavitation behaviour

To the best of the authors' knowledge, only one other study of creep cavitation in Lucalox® using SANS has been reported in the literature [12, 37]. In the work performed by Page *et al.* [12, 37], they observed that creep cavities nucleated continuously throughout the creep life of Lucalox® (where N_c/V was linear with both creep time and strain) with little subsequent cavity growth. They concluded that the time to fracture for Lucalox® was therefore governed by nucleation and not growth kinetics [12].

In this study, both the radius of gyration and Porod radius were observed to remain constant with respect to creep time and strain for all three test loads. In addition, both the volume fraction of cavities and the number of cavities per unit volume were observed to increase linearly with creep time and strain. When plotted versus creep time, the slopes of the N_c/V and V_c/V least-squares lines decreased with a decreasing applied stress. These data are all in agreement with the observations made by Page *et al.* [12, 37] and further support their conclusions that creep in Lucalox® is ruled by a cavity nucleation rather than growth process.

The effect of the magnitude of applied stress on the creep cavitation behaviour was a decrease in the slopes of the N_c/V and V_c/V versus creep time lines with decreasing applied stress. The remote applied stress is related to the localized stresses that give rise to cavitation, therefore, one would expect that as the applied stress decreased, the GBS activity (rate or sliding distance) would decrease, and creep cavitation would occur to a less severe degree. This expected decrease in cavitation is shown experimentally both as lower N_c/V and V_c/V values at a given creep time for the lower applied stress levels. In addition, the GBS rates measured at 140 and 70 MPa were 1.3×10^{-4} μm s^{-1} and 6.0×10^{-5} μm s^{-1}, respectively [1]. This decrease in GBS rate with a lower applied compressive stress is consistent with the idea that GBS is the driving force for cavitation, as resulting N_c/V and V_c/V values were lower for the 70 MPa test at a given creep time.

4.2. Correlation of GBS and creep cavitation

As discussed previously, it has been proposed by a number of researchers [9, 16, 18, 50] that the localized stresses that arise due to GBS play a direct role (acting as the driving force) in the nucleation and growth of creep cavities. Previously, direct experimental evidence for this hypothesis had been published only for metal bicrystals undergoing creep [19, 20]. Specifically, Intrater and Machlin [19] observed the number of creep cavities to increase linearly with increasing GBS displacement on copper bicrystals. In addition, Fleck *et al.* [20] also noted that the number of cavities per unit area on a grain boundary increased linearly with the magnitude of GBS displacement.

The results of this study have revealed that the number of cavities per unit volume correlate directly to the cumulative average GBS displacement, $\overline{dy}_{GB}$, as shown in Fig. 13 for polycrystalline Lucalox® undergoing creep at 140 and 70 MPa. These findings are significant, as experimental evidence now exists for a polycrystalline ceramic undergoing creep that supports the contention that GBS is the driving force for creep cavity nucleation.

Referring to the model developed by Chan and Page [51], they showed theoretically that the number of cavities nucleated per unit volume, N_c/V, is directly related to GBS displacement as follows

$$\frac{N_c}{V} = \frac{FU(t)}{\langle x \rangle} \tag{10}$$

where F is the number of cavities nucleated per unit volume in one sliding event, $U(t)$ is the average cumulative

GBS displacement, and $\langle x \rangle$ is the average sliding distance per sliding event. $U(t)$ was previously defined in Equation 5 in Part 1 [1] of this paper for the 140 MPa specimen. Therefore, Equation 10 can be altered to read

$$\frac{N_c}{V} = \frac{F[f(\overline{dy}_{GB})_{cum}]}{\langle x \rangle} \quad (11)$$

Unfortunately, F, the number of cavities nucleated per unit volume in one sliding event, is essentially an unmeasurable parameter, thus preventing a true evaluation of the model with the measured data. Nevertheless, the relationship in Equation 11 does show a direct correlation between N_c/V and $\overline{dy}_{GB}$. This correlation is also confirmed experimentally in Fig. 13 and described empirically in Equations 8 and 9. Based on the microstructural [41] and quantitative data presented for this system, it is summarized that during compressive creep, GBS appears to provide the driving force for creep cavities to nucleate, primarily on two grain facets.

The results of this work raise yet another important question; does grain boundary sliding also provide the driving force for cavity growth during creep? It is possible to use the SANS results to examine this question. If both the cavity volume fraction and the cavity density can be written in the form At^n, where t is time and A and n are constants, then the volume of an individual cavity, v, can also be expressed in this form. The constant, A, and the exponent, n, for the individual cavity volume can be determined from the requirement that, at time t

$$\frac{V_c}{V}(t) = \int_0^t A(t-t')^n \left[d\frac{N_c}{V}(t') \right] [(dt')]^{-1} dt' \quad (12)$$

The V_c/V and N_c/V data in Table I were fitted to an At^n form. Equation 12 was then solved using Equations 17 and 18 of Ref. 37 and the functional dependencies of the 100 MPa and 70 MPa V_c/V and N_c/V data. (Although the SANS generated data were used, use of the density measurement generated data would not significantly alter the results.) The 140 MPa data were excluded because of the large uncertainty in the fit brought about by the availability of only three data points. This procedure yielded an individual cavity volume that was proportional to $t^{-1.3}$ at 100 MPa and $t^{0.7}$ at 70 MPa. Differentiating with respect to time yielded the following cavity growth rates

$$\frac{dv}{dt} \propto t^{-2.5} \quad (13)$$

at 100 MPa and

$$\frac{dv}{dt} \propto t^{-0.3} \quad (14)$$

at 70 MPa.

The negative time exponents in Equations 11 and 12 are evidence of a transient growth process. Similar transient growth has been observed during compressive creep of a hot-pressed silicon carbide [38] and a liquid-phase-sintered alumina [4]. The presence of transient cavity growth suggests that the cavities are growing in response to a transient stress, such as that obtained during grain boundary sliding. It thus appears that grain boundary sliding also provides the stresses responsible for much of the cavity growth process.

The final point to be discussed relates to the relatively high applied stresses and short test times used in this study. Normal service conditions for high temperature structural components would likely use loads one or two orders of magnitude lower than those used in these experiments with components running for thousands of hours. Are the creep mechanisms observed in the accelerated tests performed representative of creep that would occur in service? Recently, tests more closely imitating service conditions have been performed on Al_2O_3 and Si_3N_4 [52]. Based on microstructural observations, the results show that GBS and creep cavitation behaviour appear to be similar to that reported here, where creep cavities nucleate, grow, and coalesce to form facet-sized cavities, and eventually lead to failure, suggesting that the accelerated tests reported here are relevant to the creep mechanisms observed in service conditions.

5. Conclusions

Creep cavitation measurements performed on specimens crept at stresses of 140, 100 and 70 MPa revealed significant information about the cavitation behavior in Lucalox®. Specifically, SANS measurements revealed that cavity volume increases linearly with specimen strain. The number of cavities per unit volume also increase with strain, while the cavity size remains constant, indicating that cavity nucleation, not growth, dominates the creep cavitation process in Lucalox® under these conditions. Cavity volume and number were shown to decrease with a decrease in applied stress.

GBS displacements measured on comparable test specimens [1] to those used in this study were correlated with results of the cavitation measurements. The direct correlation between the number of cavities nucleated per unit volume and the cumulative average GBS displacement provides experimental evidence that GBS is the driving force for creep cavity nucleation. In addition, the transient cavity growth observed suggests that GBS also appears to provide the stresses responsible for cavity growth.

Acknowledgements

The authors are grateful for the financial support of this work by the Oak Ridge Associated Universities Program and the Southwest Research Institute Internal Research Program. S.S. was supported by Oak Ridge National Laboratory, managed by Lockheed Martin Energy Research Corp. for the US Department of Energy under contract number DE-AC05-96OR22464.

References

1. C. R. BLANCHARD and R. A. PAGE, *J. Mater. Sci.* **33** (1998) 5037.

2. J. R. PORTER, W. BLUMENTHAL and A. G. EVANS, *Acta Metall.* **29** (1981) 1899.
3. K. JAKUS, S. M. WIEDERHORN and B. J. HOCKEY, *J. Amer. Ceram. Soc.* **69** (1986) 725.
4. R. A. PAGE, J. LANKFORD, K. S. CHAN, K. HARDMAN-RHYNE and S. SPOONER, *ibid.* **70** (1987) 137.
5. R. RAJ, in "Advances in fracture research," Vol. 4, edited by K. Salama, K. Ravichandar, D. M. R. Toplin and P. Rama Rao (Pergamon Press, New York, 1989) p. 2769.
6. K. S. CHAN and R. A. PAGE, *J. Amer. Ceram. Soc.* **76** (1993) 803.
7. A. G. EVANS, in "Recent Advances in creep and fracture of engineering materials and structures," edited by B. Wilshire and D. R. J. Owen (Pineridge Press, Swansea, UK 1982). p.53
8. A. H. CHOKSHI and T. G. LANGDON, *Mater. Sci. Tech.* **7** (1991) 577.
9. A. S. ARGON, I. W. CHEN and C. W. LAU, in "Creep–fatigue–environment interactions," edited by R. M. Pelloux and N. S. Stoloff (Metallurgical Society of AIME, New York, 1980) p. 46.
10. R. RAJ and M. F. ASHBY, *Acta Metall.* **23** (1975) 653.
11. D. HULL and D. E. RIMMER, *Phil. Mag.* **4** (1959) 673.
12. J. LANKFORD, K. S. CHAN and R. A. PAGE, in "Fracture mechanics of ceramics," Vol. 7, edited by R. C. Bradt, A. G. Evans, D. P. H. Hasselman and F. F. Lange (Plenum Publishing Co., New York, 1986) p. 327.
13. W. BLUMENTHAL and A. G. EVANS, *J. Amer. Ceram. Soc.* **67** (1984) 751.
14. K. S. CHAN and R. A. PAGE, *ibid.* **74** (1991) 1605.
15. T.-J. CHUANG, *ibid.* **65** (1982) 93.
16. R. RAJ, *Acta Metall.* **26** (1978) 995.
17. A. G. EVANS and A. RANA, *ibid.* **28** (1980) 129.
18. K. S. CHAN, R. A. PAGE and J. LANKFORD, *ibid.* **34** (1986) 2361.
19. J. INTRATER and E. S. MACHLIN, *ibid.* **7** (1959) 140.
20. R. G. FLECK, D. M. R. TAPLIN and C. J. BEEVERS, *ibid.* **23** (1975) 415.
21. H. GLEITER and B. CHALMERS, in "Progress in Materials Science Incorporating Progress in Metal Physics," Vol. 1b, edited by B. Chalmers, J. W. Christian and T. B. Massalski (Pergamon Press, Oxford, 1972) p. 179.
22. A. J. PERRY, *J. Mater. Sci.* **9** (1974) 1016.
23. C. R. BLANCHARD and R. A. PAGE, *ibid.* **26** (1991) 3165.
24. *Idem., J. Amer. Ceram. Soc.* **75** (1992) 1612.
25. C. R. BLANCHARD, PhD dissertation, The University of Texas at Austin, 1994.
26. S. M. COPLEY and J. A. PASK, *J. Amer. Ceram. Soc.* **48** (1965) 636.
27. J. H. HENSLAR and G. V. CULLEN, *ibid.* **50** (1967) 584.
28. T. SUGITA and J. A. PASK, *ibid.* **53** (1970) 609.
29. H. C. HEARD and C. B. RALEIGH, *Geol. Soc. Amer. Bull.* **83** (1972) 935.
30. M. TOKAR, *J. Amer. Ceram. Soc.* **56** (1973) 173.
31. T. G. LANGDON, *ibid.* **58** (1975) 92.
32. W. R. CANNON and O. D. SHERBY, *ibid.* **60** (1977) 44.
33. F. WAKAI and H. KATO, *Adv. Ceram. Mater.* **3** (1988) 71.
34. A. H. CHOKSHI, *J. Mater. Sci.* **25** (1990) 3221.
35. R. D. NIXON and R. F. DAVIS, *J. Amer. Ceram. Soc.* **75** (1992) 1786.
36. R. A. PAGE and J. LANKFORD, *ibid.* **66** (1983) C-146.
37. R. A. PAGE, J. LANKFORD and S. SPOONER, *J. Mater. Sci.* **19** (1984) 3360.
38. *Idem., Acta Metall.* **32** (1984) 1275.
39. A. S. ARGON, *Scripta Metall.* **17** (1983) 5.
40. R. A. PAGE and K. S. CHAN, *Metall. Trans. A* **18A** (1987) 1843.
41. C. R. BLANCHARD and K. S. CHAN, *J. Amer. Ceram. Soc.* **76** (1993) 1651.
42. J. R. WEERTMAN, in "Nondestructive evaluation: microstructural characterization and reliability strategies," edited by O. Buck and S. M. Wolfe, (American Institute of Mining, Metallurgical, and Petroleum Engineers, New York, NY, (1981) p. 147.
43. A. H. HEUER, N. J. TIGHE and R. M. CANNON, *J. Amer. Ceram. Soc.* **63** (1980) 53.
44. W. C. KOEHLER, *Physica* **137B** (1986) 320.
45. R. W. HENDRICKS, J. SCHELTEN and W. SCHMATZ, *Phil. Mag.* **30** (1974) 819.
46. G. D. WIGNALL and F. S. BATES, *J. Appl. Cryst.* **20** (1987) 28.
47. R. T. RATCLIFFE, *Brit. J. Appl. Phys.* **16** (1965) 1193.
48. A. GUINIER, "X-ray diffraction" (Freeman, San Francisco, 1963).
49. G. POROD, *Kolloid-Z* **125** (1952) 51.
50. A. G. EVANS, J. R. RICE and J. P. HIRTH, *J. Amer. Ceram. Soc.* **63** (1980) 368.
51. K. S. CHAN and R. A. PAGE, *J. Mater. Sci.* **25** (1990) 4622.
52. P. F. BECHER, private communication, March 15, 1994.

Received 7 February 1997
and accepted 1 June 1998